Frost halo rings beneath freezing droplets on cryogenic surfaces

Xiong Wang,[1,*,†] Zhenyue Yuan,[1] and Ran Tao[2,‡]

[1]*Department of Mechanical Engineering, City University of Hong Kong, Hong Kong 999077, People's Republic of China*

[2]*School of Physics, University of Electronic Science and Technology of China, Chengdu 611731, People's Republic of China*

(Received 25 July 2025; accepted 7 November 2025; published 18 December 2025)

We experimentally investigate the frosting phenomena beneath freezing droplets on cryogenic surfaces and reveal the emergence of previously unreported dual frost halo rings. We report that droplets impacting from low heights produce dual frost halo rings beneath the freezing droplet, whereas higher impact heights result in a single halo ring. The formation of dual halos originates from the raised bimodal morphology of the freezing droplet, which is shaped by the interplay of hydrodynamic spreading, freezing kinetics, and mechanical peeling dynamics. The locally thicker region of the raised thickness profile cools more slowly than the surrounding edge, maintaining a higher temperature that promotes localized sublimation at the freezing droplet base and subsequent vapor desublimation onto the adjacent cryogenic substrate, thereby resulting in an internal frost halo ring. Through capillary wave propagation analysis, we identify the morphology transition of different frost halo rings characterized by a power-exponent relationship between the dimensionless droplet falling height and radius. These findings provide insights into the complex interplay between capillary hydrodynamics and freezing kinetics under cryogenic conditions.

DOI: 10.1103/l61w-mj3p

I. INTRODUCTION

The spreading of droplets on undercooled surfaces represents a complex multiphysics process involving interfacial deformation, contact line dynamics, heat transfer, nucleation, and phase transition phenomena [1–5]. The intricate interplay among these mechanisms gives rise to a variety of dynamic behaviors, including but not limited to contact line pinning [6–8], formation of diverse frozen patterns [9–11], splashing enhancement [12], dendritic solid-phase growth [13,14], droplet rebound [15], and peeling effects [16,17]. These behaviors, observed across a temperature range from the freezing point of water to several tens of degrees below, have attracted sustained interest due to their potential to cause catastrophic outcomes in aviation [18], as well as their implications for icing and deicing technologies [19,20].

Despite their relevance, the spreading and freezing dynamics of droplets on cryogenic surfaces, which are typically defined as those below $-150\,^{\circ}\mathrm{C}$ and far beyond the undercooling encountered in natural systems, have received limited attention from our community. Whether such extreme thermal conditions give rise to distinct interfacial and freezing phenomena remains an open scientific question. This knowledge gap persists in part due to formidable experimental challenges, notably pervasive frosting at ultralow temperatures that hampers visualization and quantitative characterization. Despite these cryogenic processes having recently been exploited in biological contexts [21–23], their underlying dynamic mechanisms remain largely unexplored.

Here, we investigate the frosting behaviors beneath impacting droplets on cryogenic surfaces and report a previously unobserved phenomenon: The emergence of frost halo rings beneath the freezing droplet. We demonstrate how these persistent frost halos are shaped by the interplay of rapid droplet spreading, freezing kinetics, and mechanical peeling effects, which collectively determine the final morphology of the solidified droplet. Moreover, we establish a power-law scaling relationship that characterizes the transition between single- and dual-halo regimes, highlighting its dependence on droplet impact height and radius.

II. EXPERIMENTAL SETUP

The established experimental apparatus comprises a high-speed imaging system, a cryogenically cooled test stage, and a computer-controlled syringe pump for droplet generation. The imaging system integrates a Photron SA4 high-speed camera (up to 10 000 fps), a complementary CCD (coupled-charged device) camera, and a high-intensity diffuse light source, all mounted on independently adjustable platforms to enable multiangle visualization of the impact dynamics. The cryogenic test stage consists of a custom-fabricated cylindrical polystyrene insulation chamber with a transparent double-layer acrylic viewport (see Supplemental Material [24] for detailed schematics). To suppress frost formation on the optical window, the interlayer space is continuously purged with cryogenic nitrogen gas, thereby ensuring long-

*Present address: Department of Mechanical Engineering, The Hong Kong Polytechnic University, Hong Kong 999077, People's Republic of China.

†Contact author: wangxion15@tsinghua.org.cn

‡Contact author: taoran@uestc.edu.cn

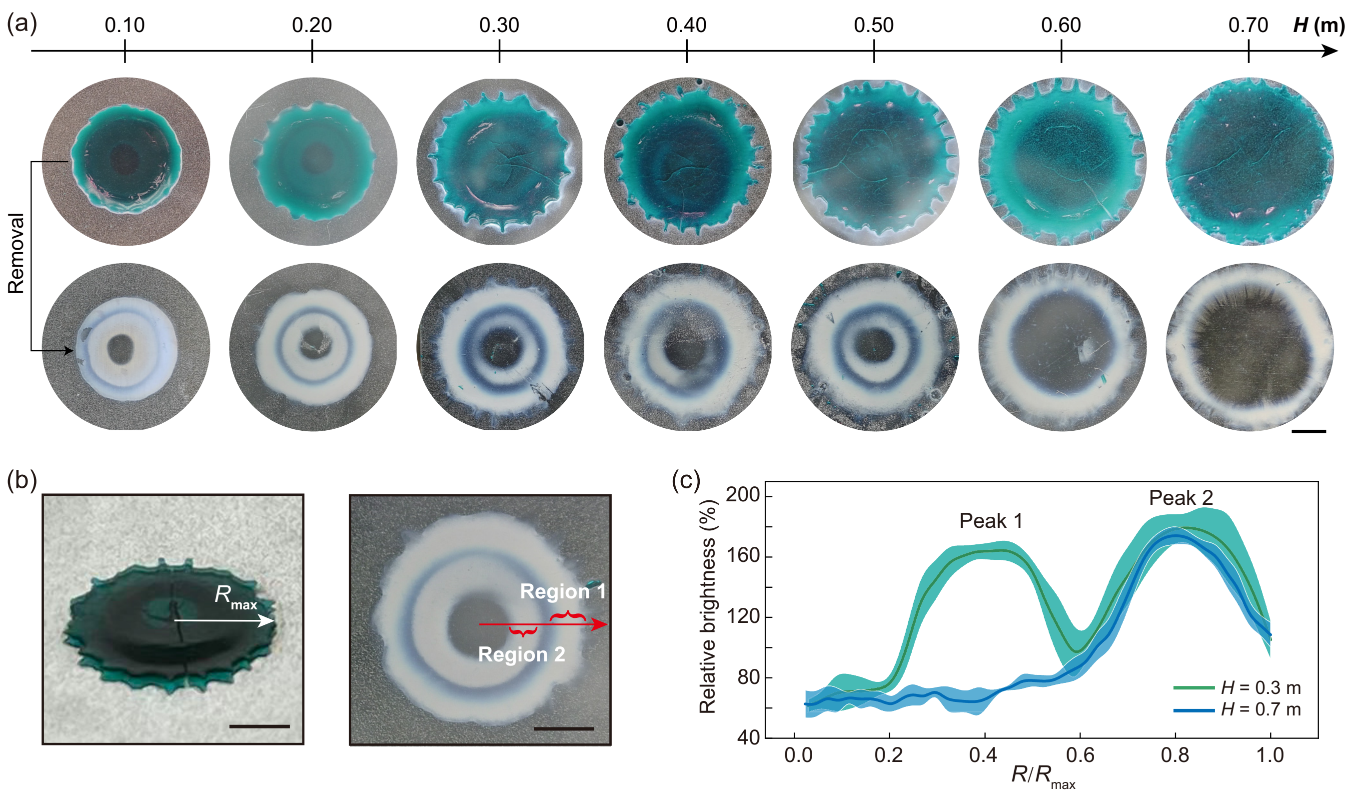

FIG. 1. (a) Morphological evolution of the freezing droplet (top row) and corresponding frost halo ring patterns beneath the droplet (bottom row) for varying droplet falling heights. (b) Image of the solidified splat formed by a droplet impacting from a falling height of 0.3 m and dual frost halo ring pattern observed on the substrate surface after removal of the solidified splat. (c) The relative brightness of the halo ring at the normalized radius (R/R_{max}) for droplets released from heights of 0.3 and 0.7 m, respectively. Scale bars in panels (a) and (b) are 2 mm.

term optical clarity. All experiments are performed inside a nitrogen-purged enclosure to eliminate interference from ambient moisture. A highly polished aluminum substrate (average surface roughness ~15 nm and thickness 3 mm) is mounted on a copper base. The substrate is positioned slightly above the insulation rim to provide an unobstructed side-view imaging path while preserving thermal isolation. Droplets are generated using an automated syringe pump with high precision, enabling accurate control of droplet radius.

The aluminum substrate is maintained at a stable temperature of $T_s = -196 \pm 2\,^\circ\text{C}$ throughout the experiments (see Supplemental Material [24] for the temperature). Gas-phase temperature, measured 1 mm above the substrate using a calibrated T-type thermocouple, indicates a stable cryogenic nitrogen environment of $-180 \pm 4\,^\circ\text{C}$. Deionized water droplets, dyed with a solid green tracer for enhanced visualization, are generated with a radius $R_0 = 1.3 \pm 0.1$ mm and an initial temperature $T_d = 25\,^\circ\text{C}$. Droplets are released from varying heights (H), resulting in impact velocities given by $U = \sqrt{2gH}$ with g representing the gravitational acceleration.

III. RESULTS AND DISCUSSION

Upon impact on the cryogenic substrate from varying heights, the droplet rapidly spreads and solidifies into a thin splat. After a sufficient cooling period exceeding 1 min, we remove the solidified splat and note that there are striking variations in the underlying frost patterns: As the falling height H increases, the pattern transitions from a dual frost halo ring structure to a single-ring morphology [Fig. 1(a)]. Specifically, when H is below 0.5 m, a distinct dual frost halo is observed; however, when H reaches 0.6 m, the pattern collapses into a single-ring morphology. It is noteworthy that droplet splashing occurs for $H \geqslant 0.2$ m (corresponding to impact velocities in the range of 1.4–2.0 m s^{-1}), consistent with prior observations by Grivet *et al.* [12], but it falls beyond the scope of the present study. Although the observed frost halos bear visual resemblance to condensation-freezing rings reported in the literature [25–28], the underlying physical mechanisms are fundamentally distinct.

To characterize these patterns, we take the dual frost halo ring structure as an example [Fig. 1(b)]. It comprises two distinct regions: an external frost halo ring (denoted by Region 1) and an internal frost halo ring (Region 2), separated by a clear, nonfrosted region. We can also quantitatively characterize these distinct frost ring patterns through radial brightness analysis [24]. As shown in Fig. 1(c), the normalized radial brightness profiles (R/R_{max}, where R_{max} is the splat radius) for droplets released from varying heights exhibit distinct features. For droplets released from $H = 0.3$ m, the brightness profile displays two well-defined peaks: an inner peak at $R/R_{max} = 0.25$–0.5, corresponding to the internal frost halo ring (Region 2), and an outer peak at $R/R_{max} \approx 0.8$, associated with the external halo ring (Region 1). A local minimum between $R/R_{max} = 0.55$–0.7 separates these two re-

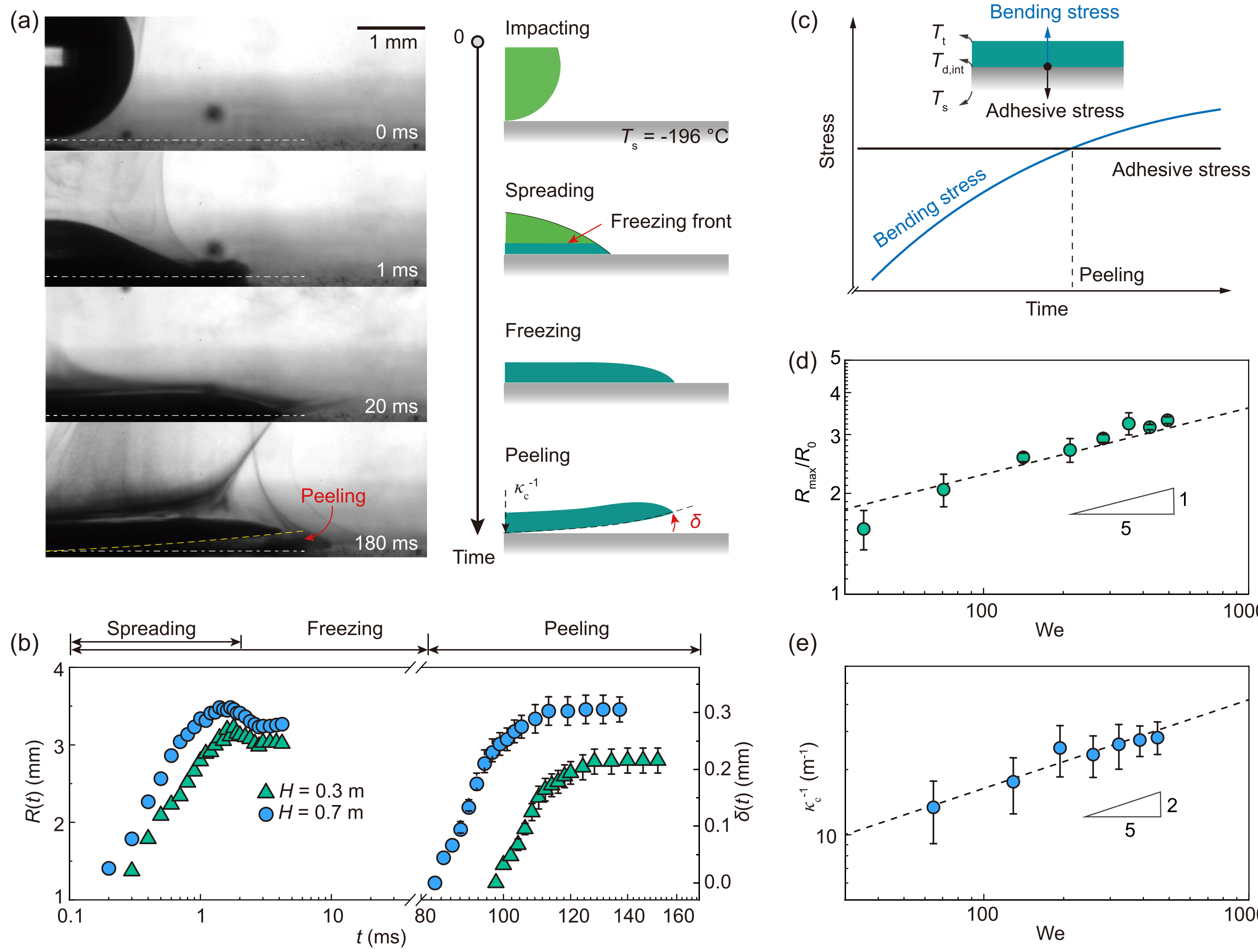

FIG. 2. (a) Selected side-view images capturing the droplet spreading and peeling dynamics after the droplet impact from a falling height of 0.3 m (left panel). Schematic illustrating the temporal evolution of the droplet through the stages of spreading, freezing, and peeling (right panel). (b) Temporal evolution of the droplet spreading radius $R(t)$ and the peeling height $\delta(t)$ of the solidified droplet. (c) Schematic representation of the vertical force balance between bending stress and adhesive stress governing the mechanical peeling of the solidified splat from the substrate. (d) Maximum spreading ratio R_{max}/R_0 as a function of We. (e) 2/5 scaling law of the bending curvature κ_c with We in Eq. (3).

gions, demarcating the dual-halo structure. In contrast, when H exceeds 0.5 m, the profile undergoes a marked transformation, collapsing into a single dominant peak at $R/R_{max} = 0.8$, signifying the disappearance of Region 2 and confirming the morphological transition observed in Fig. 1(a). These measurements provide robust, quantitative evidence for the height-dependent evolution of frost halo patterns.

To elucidate the formation of frost halo rings, we first investigate the droplet spreading and freezing dynamics through high-speed side-view imaging. When the droplet is released from $H = 0.3$ m, it undergoes a rapid spreading process, reaching its maximum radius (R_{max}) within approximately 2 ms followed by freezing into a splat [Fig. 2(a)]. Notably, the splat undergoes interfacial delamination through a peeling process after the characteristic timescale of ∼100 ms, generating a well-defined microscale gap (the edge height $\delta \approx 200$ μm) between the splat and the cryogenic surface (see Video S1 in the Supplemental Material [24]). Such peeling behavior, previously reported for high-temperature droplets impacting cold substrates [16,17,29], is attributed to thermomechanical stress mismatch during rapid solidification. The resulting detachment implies that the frost formation beneath the splat proceeds through the interstitial air gap, rather than via direct thermal conduction. Consequently, the overall droplet evolution can be delineated into three sequential regimes with initial spreading, rapid freezing, and post solidification peeling, as depicted in the right panel of Fig. 2(a).

From a timescale perspective, the three sequential yet distinct physical processes are well decoupled. We quantify each process and observe that the spreading time t_s falls within a range of 1–2 ms [Fig. 2(b)], with a timescale of $\sim 2R_0/U$. During this stage, the inertia-dominated spreading follows a characteristic power-law scaling with the spreading radius $R(t) \propto t^{0.5}$ until the contact line arrest (see Supplemental Material [24]). In contrast, the freezing process is governed by thermal diffusion. To estimate the freezing timescale, we first calculate the ratio of sensible heat to latent heat, i.e., the Stefan number $\mathrm{Ste} = c_p(T_f - T_s)/L \approx 1.23$ (T_f is the freezing temperature and L is the latent heat of ice). It indicates that the sensible heat of the droplet during freezing is comparable to its latent heat, thus needs to be considered. We therefore estimated the freezing time $t_f \sim \rho L \varepsilon^2/k(T_f - T_s)$, where ε is the thickness of the solidified splat, $k \approx 2\,\mathrm{W(m^{-1}K^{-1})}$ is ice thermal conductivity, and ρ is the density [1,14,30]. This yields an estimated t_f of about 10 ms for $H = 0.7$ m and 85 ms for $H = 0.3$ m, confirming that solidification is completed within tens of milliseconds [Fig. 2(b)]. Subsequently, the solidified splat undergoes continued cooling, leading to progressive delamination from the substrate surface.

To investigate the peeling behavior, we model the solidified splat as a thin plate. During the cooling process, the solidified splat is subjected to a vertical balance between the adhesive stress from the substrate, σ_A, and the thermal bending stress σ_κ due to its thermal gradient [29] [Fig. 2(c), inset]. Based on a scaling argument from the Griffith criterion [31,32], the adhesive stress can be expressed as

$$\sigma_{\mathrm{adh}} \propto \sqrt{\frac{\gamma_{\mathrm{is}} \times E^*}{\varepsilon}}, \tag{1}$$

where γ_{is} is the ice-substrate interfacial energy and E^* is the effective Young's modulus of the ice-substrate system. This suggests that σ_{adh} is insensitive to temperature and remains nearly constant during the cooling process [Fig. 2(c), black line], despite the material properties being dependent on the temperature. Conversely, the thermal bending stress σ_κ evolves significantly with the cooling process, which scales as $\sigma_\kappa \sim E(\alpha \Delta T)^2$ [33], where E is Young's elastic modulus, α is the thermal expansion coefficient, and $\Delta T = T_t - T_{\mathrm{d,int}}$ is the temperature difference between the top and bottom surfaces of the splat. The interfacial temperature upon droplet impact, $T_{\mathrm{d,int}}$, can be estimated by modeling the droplet and the substrate as two semi-infinite bodies brought into contact [29]. This yields the expression

$$T_{\mathrm{d,int}} = T_s + (T_d - T_s)\frac{1}{1 + e_s/e_d}. \tag{2}$$

Here, $e_i = (k\rho c_p)_i^{1/2}$ is the thermal effusivity, with subscripts s for substrate and d for droplet, and the other relevant droplet and substrate properties being conductivity k, density ρ, and heat capacity c_p. Using typical values, the calculated $T_{\mathrm{d,int}}$ is about $-92\,^\circ$C. Assuming the top surface temperature T_t remains relatively constant during the initial cooling, ΔT gradually increases as $T_{\mathrm{d,int}}$ decreases rapidly due to direct contact with the cryogenic substrate. This prediction is also confirmed by previous studies that ΔT reaches a maximum at about tens of milliseconds before decaying if no delamination occurs [34]. Consequently, σ_κ increases correspondingly [Fig. 2(c), blue line] until it exceeds the constant σ_{adh} at a critical timescale of ∼100 ms [as measured in Fig. 2(b)] and initiating peeling. Furthermore, such a stress balance framework predicts that delamination can be suppressed by reducing the thermal stress, i.e., by decreasing ΔT. This prediction is validated by replacing the aluminum substrate ($e_s \sim 20\,000\,\mathrm{W\,s^{1/2}\,m^{-2}\,K^{-1}}$) with a polycarbonate substrate ($e_s \sim 500\,\mathrm{W\,s^{1/2}\,m^{-2}\,K^{-1}}$), whose effusivity is 2 orders of magnitude lower, resulting in failed delamination in our experiment.

We also develop a scaling analysis for the bending curvature. The thermal elastic moment density of the splat scales as $M_t \sim E\varepsilon^2(\alpha\Delta T)$ [35] and the bending stiffness as $B \sim E\varepsilon^3$. Thus, the bending curvature yields $\kappa_c \sim M_t/B \sim \alpha\Delta T/\varepsilon$. By incorporating the splat thickness scaling $\varepsilon \sim \frac{R_0^3}{R_{\max}^2}$ from the volume conservation and the maximum spreading radius scaling $R_{\max}/R_0 \sim \mathrm{We}^{1/5}$ [Fig. 2(d)], we obtain the relationship

$$\kappa_c \sim \alpha\Delta T\,\mathrm{We}^{2/5}. \tag{3}$$

This theoretical prediction is well confirmed by experimental measurements of κ_c under varying We, as demonstrated in Fig. 2(e).

However, in contrast to the rapid dynamics of droplet spreading [$O(1)$ ms], freezing [$O(10)$ ms]), and mechanical peeling [$O(100)$ ms], the frost formation at cryogenic temperature (< $-190\,^\circ$C) unfolds over much longer timescales [36,37]. To elucidate the underlying mechanism of the frost formation within the confined air gap, we first consider the spatial and thermal conditions in the system. Under the cryogenic environment, the ambient pressure is below water's triple point, and the gas-phase temperature (about $-180\,^\circ$C) is far below the freezing point, which induces ice sublimation. The sublimation kinetics are accurately described by the Hertz-Knudsen equation [38], which gives the maximum theoretical mass flux J_v from a surface,

$$J_v = \beta \times (P_{\mathrm{sat}}(T) - P_\infty) \times \sqrt{\frac{M}{2\pi R_g T}}, \tag{4}$$

where β is the sublimation coefficient, $P_{\mathrm{sat}}(T)$ is the temperature-dependent saturation vapor pressure of ice, P_∞ is the ambient partial pressure of water vapor, M is the molar mass of water, R_g is the universal gas constant, and T is the absolute temperature of the local surface. Under about $-180\,^\circ$C and a pressure of 1 atm in our conditions, the ambient partial pressure of water vapor P_∞ is negligible. At the same time, the saturation vapor pressure of ice at $-180\,^\circ$C is significantly lower than 10^{-10} Pa, meaning that the ambient environment acts as a perfect sink for water vapor molecules. This simplifies the above equation, yielding

$$J_v \propto P_{\mathrm{sat}}(T) \times \sqrt{\frac{M}{2\pi RT}} \propto \frac{P_{\mathrm{sat}}(T)}{\sqrt{T}}. \tag{5}$$

To quantify this relationship and its exponential nature, we estimate $P_{\mathrm{sat}}(T)$ using the Arden-Buck equation [39], which describes its strong nonlinear dependence on temperature with

$$P_{\mathrm{sat}}(T) = 6.1115 \exp\left[\left(23.036 - \frac{T}{333.7}\right)\left(\frac{T}{279.82 + T}\right)\right]. \tag{6}$$

This underscores the exponential dependence of $P_{\mathrm{sat}}(T)$ on inverse temperature $(1/T)$. As demonstrated in Fig. 3(a), the relative sublimation rate J_v of the warmer ice sample is unequivocally and significantly faster than that of the colder one. As a result, under these extreme cryogenic conditions, frost formation is governed not by condensation and freezing, but by the direct desublimation of water vapor sublimated from the bottom surface of the splat. Therefore, the desublimation process follows a three-stage pathway as depicted in the left

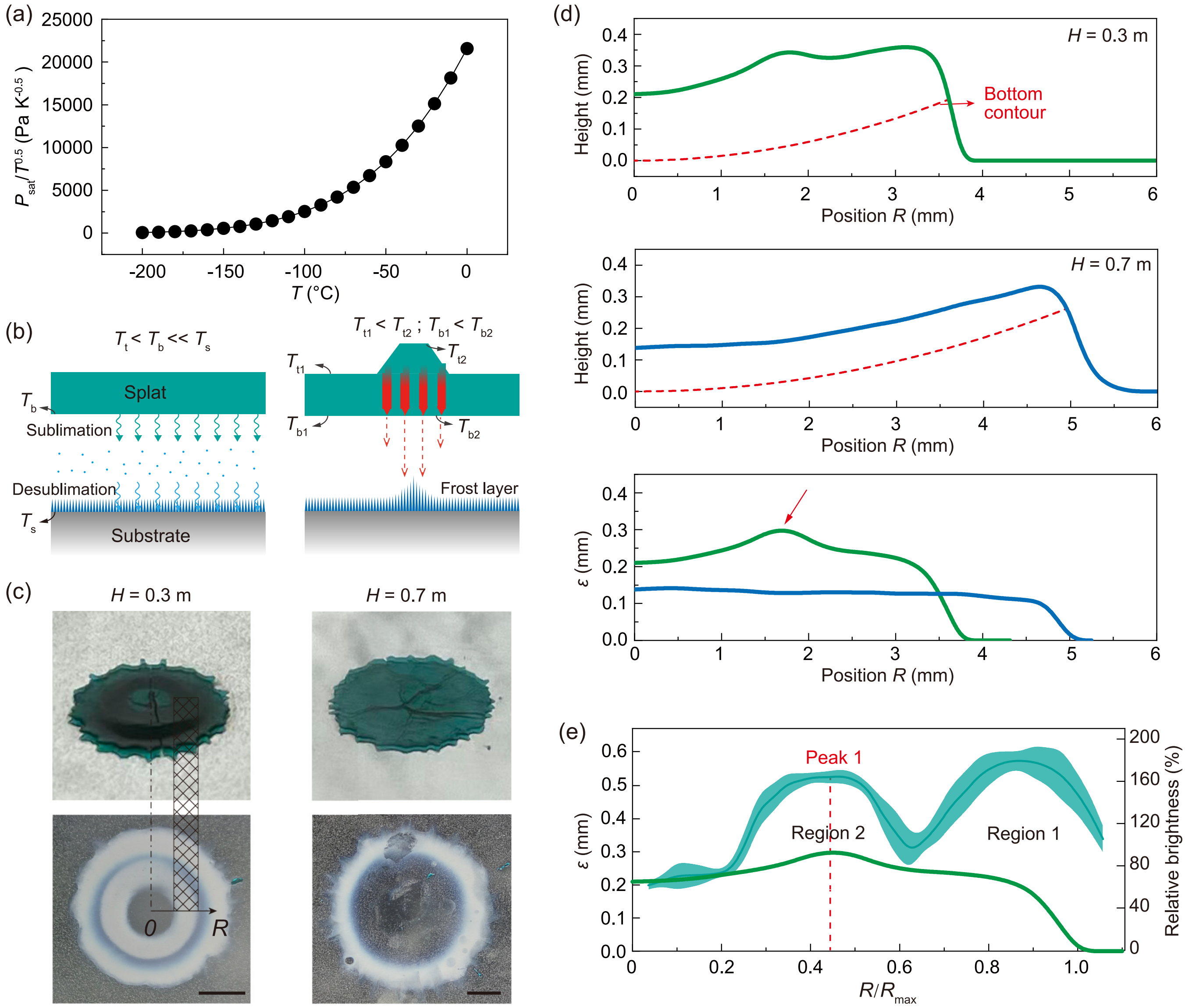

FIG. 3. (a) The relative sublimation rate $J_v \sim \frac{P_{sat}(T)}{\sqrt{T}}$ under different temperatures. (b) Schematic illustrating the formation mechanism of frost halo rings beneath the splat, driven by sublimation at the splat's base and subsequent desublimation on the cryogenic substrate. (c) Comparisons of the splat local morphology with the corresponding frost halo pattern. Scale bars: 2 mm. (d) The profile of the solidified splat formed from droplets impacting at heights of $H = 0.3$ m (top) and 0.7 m (middle), showing the local thickness ε. Actual splat thickness ε as a function of radial position (bottom). The position 0 corresponds to the splat center. Measurement uncertainty is approximately 1.0 μm. (e) Comparison of the peak position in the local profile and the frost halo ring.

panel of Fig. 3(b) [40]: (1) Sublimation of ice from the underside of the splat provides the vapor source; (2) vapor diffuses across the air gap driven by the strong gradients in vapor concentration; and (3) preferential desublimation occurs on the colder surface of the substrate. Importantly, vapor generated from both regions beneath the splat flows outward through the thin air gap. This leads to the accumulation of vapor near the periphery, where extensive desublimation occurs below the edge of the splat, resulting in the formation of Region 1 [Fig. 1(b)].

To investigate the origin of the internal frost ring (Region 2), we compare the local morphology of the splat with the corresponding frost halo pattern [Fig. 3(c)]. We note a clear correlation that the ring coincides with a distinct annular peak in the splat's thickness profile, whereas splats formed at higher impact heights exhibit flat morphology with no internal frost ring. We therefore attribute the internal frost ring primarily to these peaklike features in the splat thickness profile. Upon delamination, thicker regions cool more slowly, maintaining higher top (T_{t2}) and bottom (T_{b2}) temperatures compared to thinner areas (T_{b1} and T_{t1}), as schematized in Fig. 3(b) (right panel). The elevated temperature at the base of the thick ridge enhances localized sublimation (red arrow), producing a concentrated vapor flux that desublimates onto the substrate directly below, thereby forming the internal frost ring (Region 2).

We characterize the surface topography of the splats using a high-resolution texture analysis system (see the detailed experimental method in the Supplemental Material [24]). Figure 3(d) shows the surface profiles (solid lines) for impact

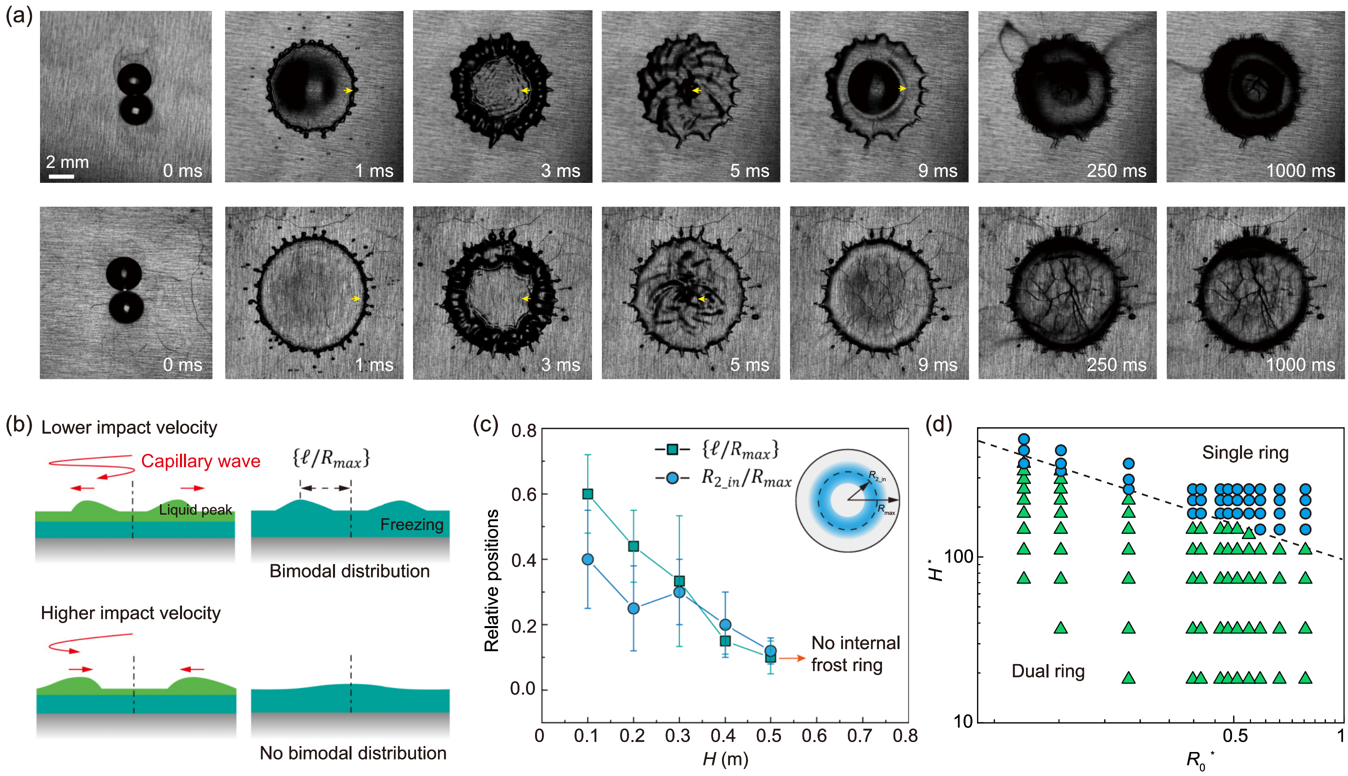

FIG. 4. (a) Selected top-view sequence images of droplet impacting on cryogenic substrates from falling heights of 0.3 m (top panel) and 0.7 m (bottom panel). The apparent bottom "double droplet" at $t = 0$ ms is an optical reflection from the mirror-smooth aluminum substrate. The yellow arrows denote the position and direction of the capillary wave fronts on the droplet surface. The black shadow region indicates the frost formation area beneath the solidified droplet. (b) Schematic of the capillary wave propagation and liquid peak moving until freezing under varying impact velocities. (c) The relative position of maximum profile thickness $\{\ell/R_{max}\}$ and the normalized peak brightness position of the internal frost ring R_{2_i}/R_{max} across different impact heights. Inset shows the schematic of the maximum brightness position of the internal frost ring R_{2_i}/R_{max}. (d) Phase diagram showing the frost halo ring morphology as a function of dimensionless impact height H^* and radius R_0^*. Blue circles represent the single frost halo ring pattern, while green triangles correspond to the dual frost halo ring pattern.

heights of 0.3 and 0.7 m. The splat formed at $H = 0.3$ m features a prominent central hump, in contrast to the uniformly concave profile observed at $H = 0.7$ m. Note that the aspect ratio is about 10, meaning that these splat structures are really flat, typically a few hundred micrometers thick and a few millimeters wide. The upper surface protrusion reaches several hundred micrometers, on the same length scale as the peeling height, which suggests that the measured profile includes a significant contribution from the air gap beneath the detached splat. Using side-view imaging, we measure the splat's lower contour and calculate the real profile of the splat at the bottom panel [Fig. 3(d), bottom panel]. We note that the splat formed at $H = 0.3$ m exhibits a hump-shaped thickness profile with bimodal distribution, whereas the splat formed at $H = 0.7$ m displays a gradually decreasing thickness with increasing radial distance. We also compared the peak position in the local profile with the frost halo ring [Fig. 3(e)]. The results show that the peak in Region 2 aligns precisely with the maximum of the profile, thereby confirming our above hypothesis.

To further substantiate the proposed mechanism, we document the dynamic evolution of droplet spreading and frost ring formation via top-view high-speed imaging. We note that capillary waves on the surface of the spreading droplet play an important role in the freezing process and the subsequent formation of the frost ring beneath it. As shown in the top panel of Fig. 4(a), the capillary wave generated by the droplet impacting from $H = 0.3$ m initially propagates outward to R_{max} and then retracts toward the center after the contact line is arrested. After completing a full round trip, the wave reverses direction and continues to propagate outward, though it does not fully reach the edge again. During this period, the freezing front advances to the free surface, leading to complete freezing at t_f. By approximately 250 ms, a distinct internal frost ring is observed precisely at the location where capillary wave propagation ceases. In contrast, the capillary wave on the surface of the droplet impacting from $H = 0.7$ m ceases during the retraction phase due to complete freezing [Fig. 4(a), bottom panel]. As a result, no internal frost ring is formed beneath it after an extended duration of approximately 1000 ms.

The interplay between the capillary wave coupled with its vertical freezing and the modal distribution profile of the splat can be understood from a theoretical perspective. The capillary wavelength on the spreading droplet is given by $\lambda = \gamma/\rho U^2$, where γ and ρ represent the surface tension and density of the droplet, respectively. Consequently, the propagation distance ℓ of the capillary wave, traveling at velocity U, scales as $\ell \sim \rho\lambda^2 U/\eta$, with η denoting the liquid viscosity [41,42]. This leads to the nonintuitive scaling $\ell \propto U^{-3}$, indicating that a lower impact velocity yields a longer capillary wave travel distance—a prediction consistent with our experimental data. Therefore, as elucidated in Fig. 4(b), at a lower impact velocity, the extended wave propagation allows the liquid peak to continue moving outward by the time freezing completes, resulting in a bimodal distribution of the splat profile. Conversely, at higher velocities, the shorter travel distance causes the liquid peak to remain in a retraction phase upon freezing, leading to a central bump. Moreover, profiles of splat formed at lower speeds exhibit a flat interior and a steep periphery, while those formed at higher speeds show a gentler slope [Fig. 3(d)]. This difference may stem from dynamic contact angle hysteresis, where the advancing contact angle exceeds the receding contact angle during the liquid peak motion [43].

We examine the correlation between the geometric profile of the splat and the optical frost pattern by comparing the relative position of maximum profile thickness, i.e., the fractional part of $\ell/R_{\max}$ denoted by $\{\ell/R_{\max}\}$, with the normalized peak brightness position of the internal frost ring $R_{2\_\mathrm{in}}/R_{\max}$ [Fig. 4(c), inset] across different impact heights H. As shown in Fig. 4(c), the two quantities match well for $H < 0.5$ m. Beyond this height ($H > 0.5$ m), the internal frost ring is no longer observable.

We further develop a scaling theory to predict the final profile based on the preceding analysis. For a large height impact, the propagation distance of the capillary wave decays rapidly, propagating a distance $\ell \sim \rho\lambda^2 U/\eta \sim 2R_{\max}$. The maximum spreading radius is known to scale as $R_{\max}/R_0 \sim \mathrm{We}^{1/5}$ [Fig. 2(d)]. From these scaling relationships, we derive a dimensionless correlation between the falling height and the droplet size,

$$H^* \sim {R_0^*}^{-12/17}, \tag{7}$$

where H^* and $D_0{}^*$ are normalized by capillary length $k_{\mathrm{capillary}}^{-1} = \sqrt{\gamma/\rho g}$ such that $H^* = H/k_{\mathrm{capillary}}^{-1}$ and $R_0{}^* = R_0/k_{\mathrm{capillary}}^{-1}$.

To validate the model, we conduct additional experiments using droplets with varying initial radii. Specifically, droplet radii ranging from 1.55 to 2.15 mm are generated using syringes equipped with different needle gauges. To produce smaller droplets (down to about 0.38 mm in radius), the syringe needles were coated with a superhydrophobic Glaco layer. The resulting phase diagram [Fig. 4(d)] reveals that the critical height for the transition between single and dual frost rings decreases exponentially with increasing normalized droplet radius $R_0{}^*$, indicating that smaller droplets require significantly higher impact velocities to yield single frost rings. The dashed line represents the power-law scaling described by Eq. (7), confirming that our theoretical framework accurately captures the underlying physics governing the frost halo transition across nearly an order of magnitude in droplet size.

IV. CONCLUSION

In summary, we investigate the frosting behavior beneath a droplet impact on a cryogenic surface and report a striking morphological transition of frost halo rings from dual rings to a single ring with increasing impact velocities. The formation of dual frost halo rings is attributed to the rapid interplay of droplet hydrodynamics, freezing kinetics, and mechanical peeling processes. In particular, the emergence of raised bimodal morphology in the solidified splat profile promotes localized sublimation at the splat's base and subsequent desublimation on the cryogenic substrate. By performing a scaling analysis of capillary wave propagation, we construct a phase diagram revealing a power-law correlation between normalized droplet falling height and radius. These findings will provide insights with potential applications in cryopreservation [21–23], cryogenic three-dimensional printing [44,45], and cryogenic manufacturing [46,47].

DATA AVAILABILITY

The data that support the findings of this article are not publicly available. The data are available from the authors upon reasonable request.

[1] M. V. Gielen, R. de Ruiter, R. B. Koldeweij, D. Lohse, J. H. Snoeijer, and H. Gelderblom, Solidification of liquid metal drops during impact, J. Fluid Mech. **883**, A32 (2020).

[2] B. Gorin, D. Bonn, and H. Kellay, Droplet impacts on cold surfaces, J. Fluid Mech. **944**, A23 (2022).

[3] I. V. Roisman, Fast forced liquid film spreading on a substrate: Flow, heat transfer and phase transition, J. Fluid Mech. **656**, 189 (2010).

[4] V. Thiévenaz, T. Séon, and C. Josserand, Solidification dynamics of an impacted drop, J. Fluid Mech. **874**, 756 (2019).

[5] A. Huerre, C. Josserand, and T. Séon, Freezing and capillarity, Annu. Rev. Fluid Mech. **57**, 257 (2024).

[6] R. De Ruiter, P. Colinet, P. Brunet, J. H. Snoeijer, and H. Gelderblom, Contact line arrest in solidifying spreading drops, Phys. Rev. Fluids **2**, 043602 (2017).

[7] R. Grivet, A. Monier, A. Huerre, C. Josserand, and T. Séon, Contact line catch up by growing ice crystals, Phys. Rev. Lett. **128**, 254501 (2022).

[8] V. Y. Lolla, S. F. Ahmadi, H. Park, A. P. Fugaro, and J. B. Boreyko, Arrested dynamics of droplet spreading on ice, Phys. Rev. Lett. **129**, 074502 (2022).

[9] V. Thiévenaz, C. Josserand, and T. Séon, Retraction and freezing of a water film on ice, Phys. Rev. Fluids **5**, 041601 (2020).

[10] W.-Z. Fang, F. Zhu, W.-Q. Tao, and C. Yang, How different freezing morphologies of impacting droplets form, J. Colloid Interface Sci. **584**, 403 (2021).

[11] E. Ghabache, C. Josserand, and T. Séon, Frozen impacted drop: From fragmentation to hierarchical crack patterns, Phys. Rev. Lett. **117**, 074501 (2016).

[12] R. Grivet, A. Huerre, T. Séon, and C. Josserand, Making superhydrophobic splashes by surface cooling, Phys. Rev. Fluids **8**, 063603 (2023).

[13] P. Kant, H. Müller-Groeling, and D. Lohse, Pattern formation during the impact of a partially frozen binary droplet on a cold surface, Phys. Rev. Lett. **125**, 184501 (2020).

[14] P. Kant, R. B. Koldeweij, K. Harth, M. A. van Limbeek, and D. Lohse, Fast-freezing kinetics inside a droplet impacting on a cold surface, Proc. Natl. Acad. Sci. USA **117**, 2788 (2020).
[15] V. Kulkarni, S. Tamvada, N. Shirdade, N. Saneie, V. Y. Lolla, V. Batheyrameshbapu, and S. Anand, Increased solidification delays fragmentation and suppresses rebound of impacting drops, Phys. Rev. Fluids **9**, 053604 (2024).
[16] P. Jin *et al.*, Ultra-low ice-substrate adhesion and self-deicing during droplet impact freezing, Cell Rep. Phys. Sci. **3**, 100894 (2022).
[17] W.-Z. Fang, F. Zhu, L. Zhu, W.-Q. Tao, and C. Yang, Self-peeling of frozen water droplets upon impacting a cold surface, Commun. Phys. **5**, 51 (2022).
[18] T. Cebeci and F. Kafyeke, Aircraft icing, Annu. Rev. Fluid Mech. **35**, 11 (2003).
[19] A. Dhyani, W. Choi, K. Golovin, and A. Tuteja, Surface design strategies for mitigating ice and snow accretion, Matter **5**, 1423 (2022).
[20] M. J. Kreder, J. Alvarenga, P. Kim, and J. Aizenberg, Design of anti-icing surfaces: Smooth, textured or slippery? Nat. Rev. Mater. **1**, 1 (2016).
[21] Y. Akiyama, M. Shinose, H. Watanabe, S. Yamada, and Y. Kanda, Cryoprotectant-free cryopreservation of mammalian cells by superflash freezing, Proc. Natl. Acad. Sci. USA **116**, 7738 (2019).
[22] U. Demirci and G. Montesano, Cell encapsulating droplet vitrification, Lab Chip **7**, 1428 (2007).
[23] R. Dou, R. E. Saunders, L. Mohamet, C. M. Ward, and B. Derby, High throughput cryopreservation of cells by rapid freezing of sub-μl drops using inkjet printing–Cryoprinting, Lab Chip **15**, 3503 (2015).
[24] See Supplemental Material at http://link.aps.org/supplemental/10.1103/l61w-mj3p for additional details, which include the cold stage, image processing, spreading law, and Video S1.
[25] S. Zhen, H. Feng, S. Lin, Y. Jin, Z. Li, X. Deng, E. Bonaccurso, and L. Chen, Condensate halos in condensation frosting, Adv. Sci. **12**, 2410657 (2025).
[26] Y. Zhao, F. Zhu, H. Zhang, T. H. New, L. Jin, and C. Yang, Triple condensate halo from a single water droplet impacting upon a cold surface, Appl. Phys. Lett. **114**, 183703 (2019).
[27] S. Kavuri, G. Karapetsas, C. S. Sharma, and K. C. Sahu, Freezing of sessile droplet and frost halo formation, Phys. Rev. Fluids **8**, 124003 (2023).
[28] S. Jung, M. K. Tiwari, and D. Poulikakos, Frost halos from supercooled water droplets, Proc. Natl. Acad. Sci. USA **109**, 16073 (2012).
[29] J. de Ruiter, D. Soto, and K. K. Varanasi, Self-peeling of impacting droplets, Nat. Phys. **14**, 35 (2017).
[30] A. Bejan, *Convection Heat Transfer* (John Wiley & Sons, New York, 2013).
[31] A. A. Griffith, VI. The phenomena of rupture and flow in solids, Philos. Trans. R. Soc. London, Ser. A **221**, 163 (1921).
[32] T. L. Anderson and T. L. Anderson, *Fracture Mechanics: Fundamentals and Applications* (CRC Press, Boca Raton, Florida, 2005).
[33] J. W. Hutchinson and Z. Suo, Mixed mode cracking in layered materials, Adv. Appl. Mech. **29**, 63 (1991).
[34] S. Sundaram, D. Lipkin, C. Johnson, and J. W. Hutchinson, The influence of transient thermal gradients and substrate constraint on delamination of thermal barrier coatings, J. Appl. Mech. **80**, 011002 (2013).
[35] A. F. Bower, *Applied Mechanics of Solids* (CRC Press, 2009).
[36] P. Kékicheff *et al.*, Condensation or desublimation: Nanolevel structural look on two frost formation pathways on surfaces with different wettabilities, ACS Nano **18**, 15067 (2024).
[37] F. Wang, R. Tang, Z. Wang, and W. Yang, Frosting characteristics of superhydrophobic surface under desublimation frosting conditions, Int. J. Therm. Sci. **184**, 108038 (2023).
[38] A. H. Persad and C. A. Ward, Expressions for the evaporation and condensation coefficients in the Hertz-Knudsen relation, Chem. Rev. **116**, 7727 (2016).
[39] A. L. Buck, New equations for computing vapor pressure and enhancement factor, J. Appl. Meteorol. Climatol. **20**, 1527 (1981).
[40] C. Walker, S. Lerch, M. Reininger, H. Eghlidi, A. Milionis, T. M. Schutzius, and D. Poulikakos, Desublimation frosting on nanoengineered surfaces, ACS Nano **12**, 8288 (2018).
[41] Y. Renardy *et al.*, Pyramidal and toroidal water drops after impact on a solid surface, J. Fluid Mech. **484**, 69 (2003).
[42] X. Wang, X. Yan, J. Du, B. Ji, M. J. Inanlu, Q. Min, and N. Miljkovic, Spreading dynamics of microdroplets on nanostructured surfaces, J. Colloid Interface Sci. **635**, 221 (2023).
[43] P. G. D. Gennes, Wetting: Statics and dynamics, Rev. Mod. Phys. **57**, 827 (1985).
[44] M. Adamkiewicz and B. Rubinsky, Cryogenic 3D printing for tissue engineering, Cryobiology **71**, 518 (2015).
[45] Z. Li, M. Xu, J. Wang, and F. Zhang, Recent advances in cryogenic 3D printing technologies, Adv. Eng. Mater. **24**, 2200245 (2022).
[46] Y. Kakinuma, S. Kidani, and T. Aoyama, Ultra-precision cryogenic machining of viscoelastic polymers, CIRP Ann. **61**, 79 (2012).
[47] M. Liu *et al.*, Cryogenic minimum quantity lubrication machining: From mechanism to application, Front. Mech. Eng. **16**, 649 (2022).